

Landslides (2023) 20:2657–2674
 DOI 10.1007/s10346-023-02121-8
 Received: 1 March 2023
 Accepted: 21 July 2023
 Published online: 5 August 2023
 © Springer-Verlag GmbH Germany,
 part of Springer Nature 2023

G. Walton · C. Christiansen · R. Kromer · A. Silaev

Evaluation of rockfall trends at a sedimentary rock cut near Manitou Springs, Colorado, using daily photogrammetric monitoring



Evaluation of rockfall trends at a sedimentary rock cut

Abstract Rockfall remains a prominent hazard for transportation corridors worldwide. Recent studies have shown promising results in resolving the relationships between rockfall activity and triggers, including in some cases detecting precursor activity prior to failure, which could have implications to improving safety and performance of transportation corridors. The aim of this study is to better understand rockfall failure processes and triggers for cut slopes in interbedded sedimentary rock through a long-term study using photogrammetry data with high spatiotemporal frequency. The combination of daily data, high-precision rockfall volume estimation, and 22-month monitoring duration is unique among studies that evaluate rockfall triggers and allows us to derive insights into differences in rockfall triggering between blocks of different volumes. The data collected allowed the relative frequency of rockfalls of different volumes to be well-constrained for volumes ranging from 0.01 m³ up to 76 m³ (the largest event that occurred during the monitoring period). A quantitative comparison between precipitation and rockfall activity established that precipitation was the primary trigger for rockfall at the site, with only 1.4% of 24-h photo intervals without precipitation having at least one rockfall, as compared to 25.0% of photo intervals with precipitation (and 57.1% of photo intervals with at least 5 mm of precipitation). The marginal impact of additional rainfall above 8 mm per 24-h period on rockfall probability was negligible among all rockfalls observed, whereas the probability of the largest rockfalls at the site (> 1 m³) occurring continued to increase as a function of precipitation up to 20 mm per 24-h period. Detailed analysis of change data leading up to the largest (76 m³) rockfall observed illustrated the progressive failure mechanism of the block, including observations of forward toppling motion and smaller precursor rockfalls around its perimeter. This rockfall was also used for a proof-of-concept demonstration of the potential for a spatiotemporal rockfall density metric to be used to help identify areas of potential hazard. Ultimately, the findings from this study contribute to knowledge on rockfall processes outside alpine regions, which have historically been less well-studied.

Keywords Rockfall · Photogrammetry · Precursors · Progressive failure · Triggers

Introduction

Rockfall is a hazard that is present in mountainous terrain around the world, and the Colorado Rockies are no exception. While the processes and environmental factors that lead to rockfall have been

widely studied (e.g. Matsuoka and Sakai 1999; Paranunzio et al. 2016; Weidner and Walton 2021; Mourey et al. 2022), the relative importance of different processes and factors varies significantly depending on climate and rockmass characteristics. This variation means that even if the general mechanics of rockfall and associated triggering processes are understood, further studies are needed to evaluate the differences in observed phenomena for specific slopes in a variety of regions. Additionally, improvements in data collection approaches now allow for rockfall phenomena to be studied with greater resolution and precision than was previously possible.

Over the past decade, the Colorado Department of Transportation has invested in the development and deployment of remote sensing technologies to monitor, evaluate, and forecast rockfall hazards. This is consistent with the broader trend of LiDAR and structure-from-motion (SfM) photogrammetry being increasingly applied in the field of rockfall monitoring research (Abellán et al. 2014; Eltner et al. 2016; van Veen et al. 2017; Williams et al. 2019; Weidner and Walton 2021). In this case, we have utilized a previously developed fixed photogrammetric monitoring approach (Kromer et al. 2019) to collect high spatiotemporal resolution monitoring data and develop a novel rockfall database spanning 22 months with daily resolution. This database is unique, in that most existing studies on rockfall processes focus on slopes above the permafrost limit and rely on short or incomplete rockfall records (Mainieri et al. 2023), whereas this study focuses on an interbedded sedimentary rock cut in a non-alpine, “Humid Continental (NOAA 2022) environment.” The goal of this study is to use this database to develop insights regarding rockfall mechanisms, triggers, and precursors to eventually inform geotechnical asset management practices.

Background and research objectives

Photogrammetry is commonly used to study slope characteristics and landscape evolution, including rockmass structural mapping (e.g., Salvini et al. 2017; Calì et al. 2023), change detection in glacial environments (Śledź et al. 2021), rockfall trajectory evaluation (e.g., Sarro et al. 2018; Gallo et al. 2021; Robiati et al. 2023), rockfall hazard evaluation (e.g., Vanneschi et al. 2019; Guerin et al. 2020; Janeras et al. 2023), and evaluation of rockfall processes and controlling factors (e.g., Fleischer et al. 2023; Graber and Santi 2023). Regarding the study of rockfall processes specifically, other methods have historically been used to develop rockfall databases, including manual collection of fallen

rock debris (e.g., Matsuoka and Sakai 1999; Imaizumi et al. 2020), visual analysis of time lapse or stereoscopic photographs (e.g., D'Amato et al. 2016; Matsuoka 2019), dendrochronology (e.g., Stoffel et al. 2005; Zielonka and Wrońska-Walach 2019), review of historical reports (e.g., Delonca et al. 2014; Macciotta et al. 2015; Banji et al. 2021), and repeated laser scanning (e.g., van Veen et al. 2017; Williams et al. 2019; Weidner and Walton 2021; Birien and Gauthier 2023). Several prior studies evaluating rockfall processes have developed large databases spanning long time periods and used these databases to establish freeze–thaw, precipitation, and wildfire impacts on rockfall hazard. These longer-term studies tend to use longer monitoring intervals, and as a consequence, associating a specific trigger event with the precise timing of a rockfall becomes difficult (e.g., Hartmeyer et al. 2020; Weidner and Walton 2021; Graber and Santi 2023; Birien and Gauthier 2023). Studies that have evaluated rockfall triggers using databases with precise rockfall timing have typically not considered differences in rockfall trends depending on block size (e.g., Delonca et al. 2014; D'Amato et al. 2016). Studies employing shorter monitoring intervals (on at least a daily basis) have yet to be widely applied over the long term (> 1 year) but have shown promise in detecting smaller magnitude rockfalls, evaluating rockfall triggers, and analyzing precursor activity (e.g., Kromer et al. 2017; Williams et al. 2019; Giacomini et al. 2020; Mourey et al. 2022; Nunez-Andrés et al. 2023).

In evaluating rockfall triggers and precursors (e.g., peripheral rockfalls or block movement), high spatial resolution is critical to allow the smallest (most frequent) rockfalls to be detected, spatial relationships between distinct rockfall events to be identified, and rockfall volumes to be reliably established. Additionally, high temporal resolution is necessary to allow for the timing of individual rockfalls to be more precisely correlated to the occurrence of potential triggering events (Williams et al. 2019). Accordingly, various researchers have worked to develop advancements in data collection and processing workflows to enable high spatiotemporal resolution data collection and analysis using LiDAR (Kromer et al. 2017; Williams et al. 2019; Anders et al. 2021) and photogrammetry systems (Roncella and Forlani 2015; Santise et al. 2017; Eltner et al. 2017; Parente et al. 2019; Kromer et al. 2019; Blanch et al. 2020, 2021; Núñez-Andrés et al. 2023).

In this study, we use a system based on the one developed and deployed by Kromer et al. (2019) along the Interstate-70 highway through Colorado to develop daily photogrammetry models for rockfall detection based on its ability to automatically collect and process photogrammetric data, as well as its relatively low cost and high degree of automation (we refer the reader to Kromer et al. 2019 for a full description of the applicability of the system and comparison with alternatives). Our aim is to use a high spatial temporal resolution rockfall database collected through daily fixed photogrammetric monitoring to get unique insights into the rockfall behavior at the slope including any triggering factors and precursory activity. Specifically, our research focuses on answering the following questions:

- What factors are triggering rockfalls at this site, and over what timescales are these factors acting? How does this relate to findings regarding triggers at other slopes with different geological and climatic characteristics?

- Are there variations in rockfall triggers and/or mechanisms as a function of block size?
- What kinds of precursors to rockfalls can be detected using this type of monitoring approach?
- How can high-resolution point cloud models be used to evaluate the spatiotemporal evolution of rockfall hazard across the slope?

Answering these questions to advance understanding of rockfall processes in great detail as enabled by our high spatiotemporal resolution database can contribute to interpretation of slope behavior and the management of slope hazards more broadly. For example, in a geotechnical asset management context, obtaining a better understanding of slope deterioration rates at cut slopes can be used to optimize slope maintenance activities, and detecting precursor activity can also guide the allocation of resources for more immediate hazard mitigation efforts, which will ultimately improve asset performance.

We note that while previous studies have attempted to answer similar questions in the context of different study sites and methods, our study is distinct in two main ways: (1) the combination of geological (interbedded mudstone-sandstone), geotechnical (cut slope rather than natural), and climatic conditions is unique relative to other related studies in the literature; (2) the extended monitoring length (22 months) and high temporal resolution (day-to-day change detection) used for this study combined with the evaluation of individual rockfall volumes allows for analyses to be conducted that would not have been possible (or prohibitively costly or time consuming) using most alternative methods for rockfall database development.

Methods

Site description

The slope of interest for this study is a near-vertical (75°) rock cut on the north side of US highway 24 in Manitou Springs, Colorado. The location of the slope is shown in Fig. 1, and 2 illustrates the monitored area, which covers approximately 2500 m² of rock slope. A ditch is positioned beneath the slope to minimize the potential for rockfall from the slope to reach the highway.

The slope consists of interbedded arkosic sandstones and mudstones of the Fountain Formation in foothills of the Rocky Mountains. This formation is of Pennsylvanian-Permian age and was formed by lithification of sediments eroded from the Ancestral Rocky Mountains. Based on variations in depositional conditions over time and space, the formation includes a variety of distinct lithologies, with conglomerate and sandstone being most prominent. The absence of conglomerate and presence of mudstone beds at our study site suggest that the sediments were deposited under lower energy conditions than much of the formation (Sweet et al. 2015). The thickness of the beds is highly irregular, ranging from a few centimeters to multiple meters, although the sandstone beds are typically thicker than the mudstone beds. Although strength data for the intact sandstone and mudstone units are not available, it is clear that the mudstone is much weaker than the sandstone, as significant differential erosion is visible on the slope, which leads to the occurrence of overhanging sandstone layer geometries.

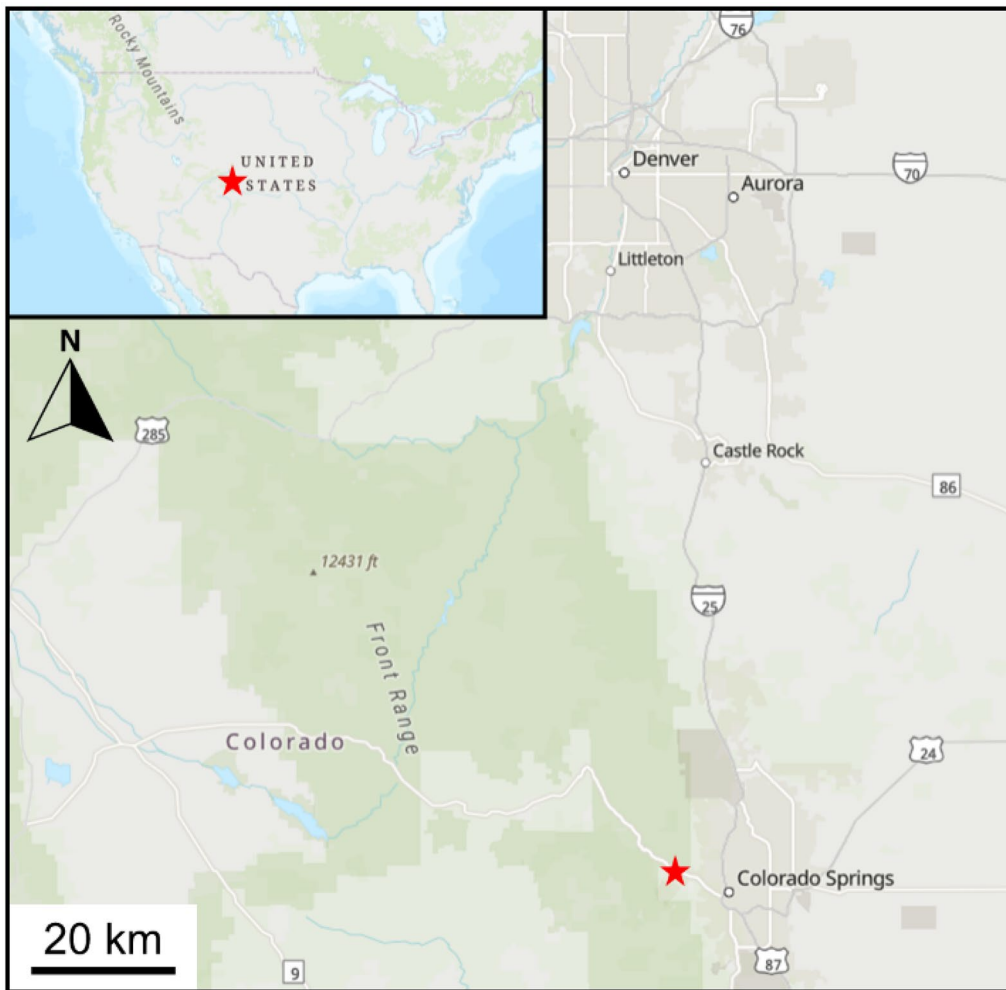


Fig. 1 Site location approximately 5 km west of Colorado Springs on highway US-24 (Esri 2022)

Figure 3 presents an annotated photo of the slope with key rockmass features highlighted. The primary fractures present in the slope correspond to highly persistent sub-horizontal bedding planes that dip shallowly to the northeast. Two sets of sub-vertical cross joints are also present, with average dip directions towards

the NNE and E. The cross-joint spacing is highly variable between different layers (see Fig. 3) and ranges from a few centimeters to multiple meters. The joints are typically fresh to slightly weathered and primarily planar and rough, with some joints exhibiting an undulating-rough character (ISRM 1978).

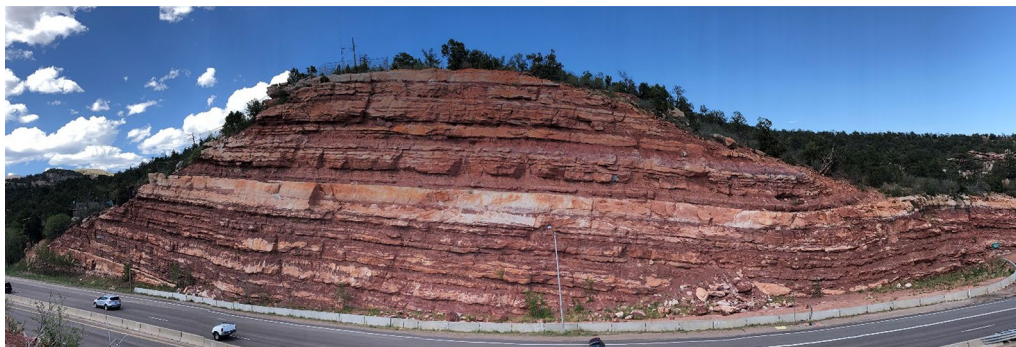


Fig. 2 Panorama view of the monitored slope

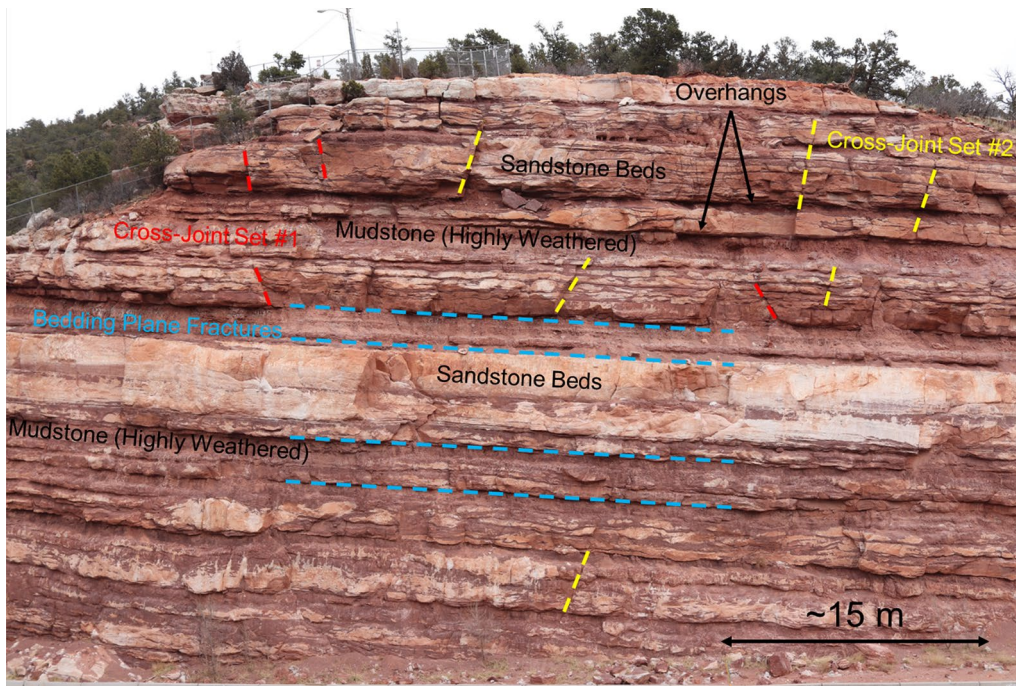


Fig. 3 Annotated slope photograph illustrating key rockmass features

Photogrammetry data collection and processing workflow

On January 24, 2020, five fixed camera stations were installed opposite the target slope (see Fig. 4) at a distance of approximately 60 m. The system design was based on that of Kromer et al. (2019). Each station consists of a camera (Canon T7i) and lens (24 mm focal length), a solar panel, an internal battery pack, a microcomputer controller, a wireless internet connection, and a weatherproof and tamperproof protective housing.

Starting on 2020 January 24, each camera was set to capture photos at noon and 12:30 pm each day. This study presents an analysis of the data collected between 2020 January 24 and 2021 November 30.

Each day, each station's USB LTE modem uploaded the photos to an FTP server. A scheduled program was then set to run the subsequent data processing steps, including SfM model construction, automated registration with scale, vegetation removal, and change calculation. The overall workflow matches that described in detail by Kromer et al. (2019) and is represented by the flowchart in Fig. 5. Camera calibration parameters were estimated during construction of the initial baseline model and were fixed for all subsequent models to maximize change detection precision (e.g., by ensuring any distortion effects remain consistent from day to day) (Kromer et al. 2019). A terrestrial laser scan was collected using a Faro Focus 3D × 330 scanner at the start of the monitoring period, and the corresponding point cloud was used for scaling and referencing of the initial baseline photogrammetry model. Differences between the LiDAR point cloud and the initial photogrammetric model (i.e., with negligible real slope change) had a standard deviation of 3 cm (representative of photogrammetric model accuracy), with the largest differences occurring towards the edges of the photogrammetric model due to distortion effects, likely caused by a lower degree of photo overlap than in the central part of the slope. Comparisons between photogrammetric models with consistent camera

calibration parameters (per Kromer et al. 2019) revealed a smaller standard deviation, typically on the order of 1.5 cm (representative of change detection precision); this lower standard deviation

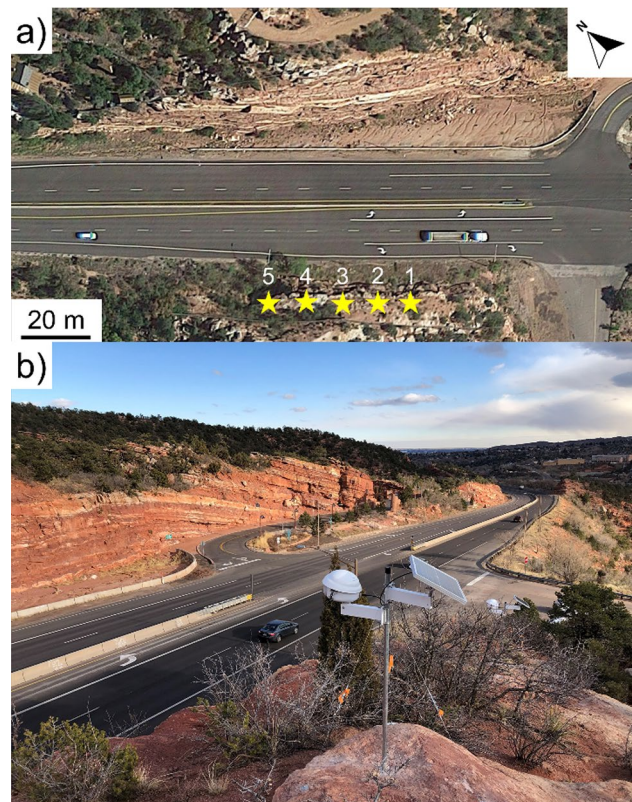


Fig. 4 Images illustrating **a** camera locations shown with stars and camera numbers in white and **b** close-up view of camera station 2, looking eastward

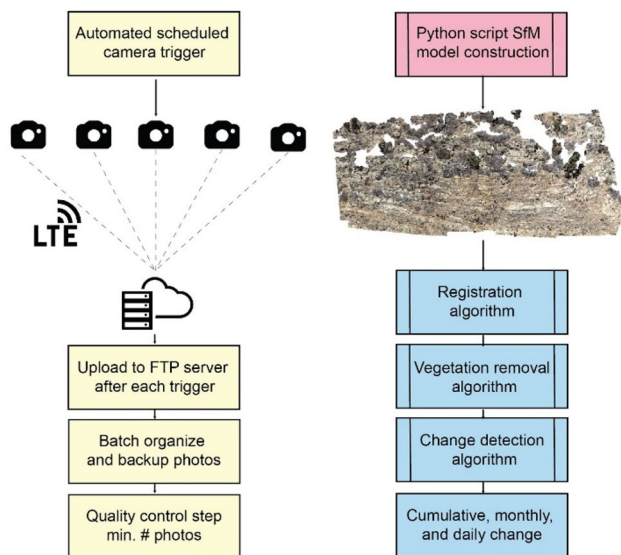


Fig. 5 Data processing pipeline from data collection to production of change detection results (Kromer et al. 2019)

is a function of broad photogrammetric distortion effects remaining consistent between day-to-day photogrammetric models and therefore not influencing localized change results (or associated rockfall detection).

Rockfall identification

Change maps produced by the automated process described in the “[Photogrammetry data collection and processing workflow](#)” section were reviewed a minimum of once per week to manually interpret the causes of the apparent changes on the slope. While large rockfalls were immediately clear from the change maps, smaller areas of apparent change needed to be manually assessed to determine whether they represented rockfall or noise (due to, for example, local photogrammetry model distortion or residual unmasked areas of vegetation). Approximate volumes for all change regions identified to represent rockfall were estimated using the 2.5-dimensional volume calculation tool built into CloudCompare because of its ease of use during routine visualization and interpretation of results (CloudCompare 2019). While this method is likely to tend to overestimate volumes in contrast to more sophisticated volume calculation approaches, we note that while the absolute volume estimates should not be considered precise, the relative volume trends that are the focus of this study are expected to be reliable (DiFrancesco et al. 2021).

In addition to evaluating the regularly produced change maps, the raw photographs themselves were also inspected in detail to avoid missing rockfalls. This was critical, particularly because some rockfalls that failed to register a detectable change in the comparison of photogrammetry models were noted to be visually observable in the raw photographs collected by the monitoring system. The reason for increased resolvability of rockfall events in the photographs is that the process of converting two-dimensional

images into a three-dimensional photogrammetry model is inherently associated with a loss of resolution and an increase in uncertainty due to smoothing, filtering, and downsampling during image matching as well as the introduction of survey and algorithmic uncertainty (James et al. 2017). Although specific volumes could not be estimated for the smallest rockfalls identified strictly from the photographs, based on their areal extents and the typical surface-area-to-volume ratios calculated for larger rockfalls, these rockfalls were recorded as having a volume of less than 0.01 m^3 (approximately 0.4 ft^3); for the purposes of analyses considering total daily rockfall volumes, these smaller rockfalls were assigned a volume of 0.005 m^3 . Note that regions of channelized erosion in the weaker mudstone layers visible in some of the photos were not recorded with the rockfalls and not included in any volume calculations.

Potential rockfall triggers—weather data

To allow for comparison of observed rockfall trends with weather patterns at the site, a meteorological data set was retrieved from an online weather data repository (Weather Underground 2021). Specifically, data from a WS-2902 weather station located approximately 1.1 km south of the monitoring system and at the same elevation (1,980 m) was used (Station ID: KCOMANIT26). The dataset includes temperature, cumulative precipitation, and precipitation rate data. Data were recorded by the weather station at an interval of 5 min. Raw temperature and precipitation data for the study period are presented in Fig. 6.

One major limitation of the type of weather station used is that snow is not accounted for in the precipitation totals recorded (Ambient Weather 2018); this is reflected in the negligible precipitation totals shown during the winter months in Fig. 6.

To evaluate the potential influence of snowmelt on rockfall at the site, photos were visually examined to evaluate the presence or absence of snow on (or above) the slope for each day of the study period. Based on this visual examination, photo intervals where the amount of snow on the slope was observed to decrease (i.e., indicating snowmelt) were noted.

Note that seismicity was not considered as a potential significant rockfall trigger at the study site, as the region is not highly seismically active; only one event with magnitude > 1.0 occurred within 30 km of the study site during the study period, and the largest event within 150 km of the study site during the study period had a magnitude of 2.5 (USGS 2022).

Development of a spatiotemporal rockfall density metric

To aid in the interpretation of the rockfall data collected, a spatiotemporal rockfall density metric (conceptually similar to Anders et al. 2020) was developed. Such a metric is of interest because clustering of smaller rockfalls (in both space and time) can precede larger rockfall events (Rosser et al. 2007; Royán et al. 2014, 2015; Kromer et al. 2015); therefore, a method that can be used to identify such precursory spatiotemporal clustering of rockfalls may be used in the assessment and management of future rockfall hazard.

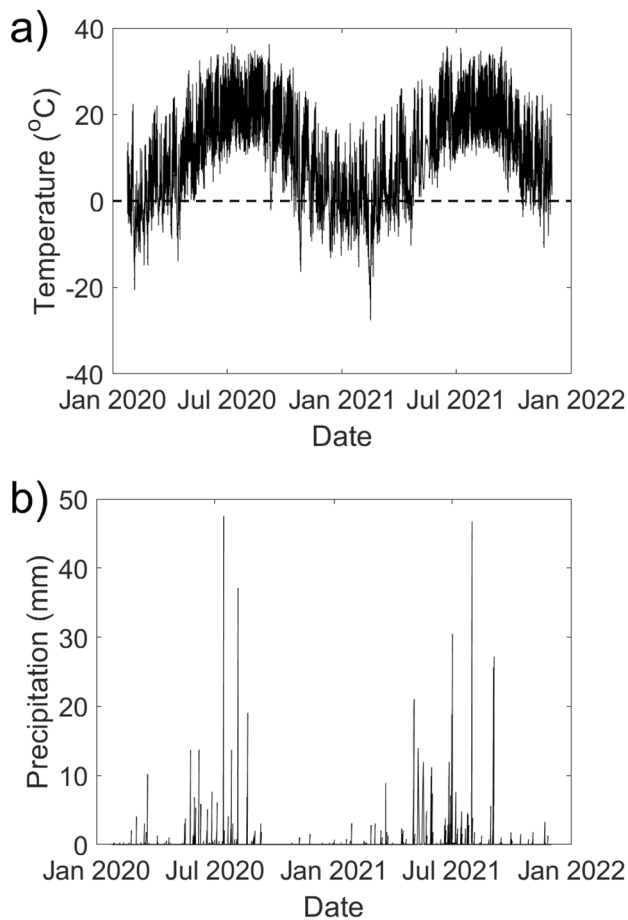


Fig. 6 Temperature and precipitation data for the study period from a weather station located ~1.1 km from the monitoring site

To calculate the rockfall density metric, the slope was first discretized into a two-dimensional grid consisting of $1\text{ m} \times 1\text{ m}$ grid cells (see Fig. 7). Every rockfall was assigned to a grid cell; note that the uncertainty in positioning rockfalls visually identified from photographs is a major reason why a grid size smaller than $1\text{ m} \times 1\text{ m}$ was not considered.

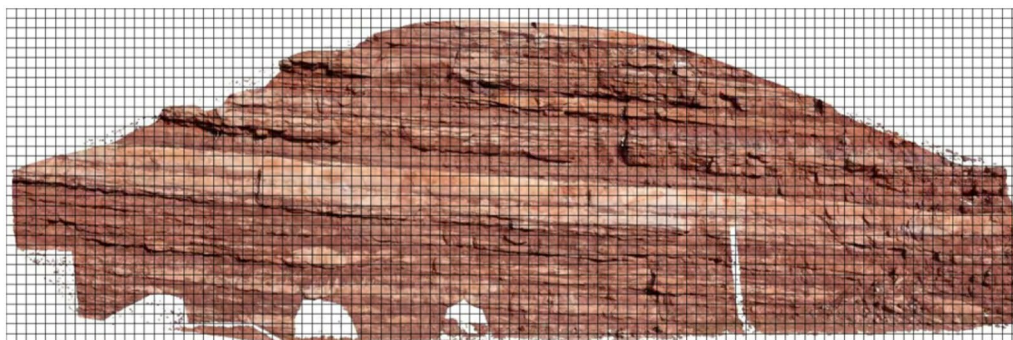


Fig. 7 Gridded view of the monitored slope

For every day of the study period and every grid cell, the spatiotemporal rockfall density metric was calculated according to the following equation:

$$STRFD(x, z, t) = \frac{\sum_{i=1}^n \left(\frac{1}{\sqrt{(x-x_i)^2 + (z-z_i)^2}^a} \cdot \frac{1}{(t-t_i)^b} \right)}{\sum_{j=1}^m \sum_{k=1}^p \left(\frac{1}{\sqrt{(x-x_j)^2 + (z-z_j)^2}^a} \cdot \frac{1}{(t-t_k)^b} \right)} \quad (1)$$

where the variables in this equation are defined as follows:

- STRFD = spatiotemporal rockfall density
- x = the horizontal coordinate of the centroid of a given cell of interest
- z = the vertical coordinate of the centroid of a given cell of interest
- t = a given date of interest
- a = distance weighting coefficient
- b = time weighting coefficient
- i = counter for rockfalls
- n = total number of rockfalls as of date “ t ”
- j = counter for grid cells
- m = total number of grid cells covering the outcrop (not including blank cells around edges)
- k = counter for days
- p = total number of days from the start of monitoring to date “ t ”

The numerator of the equation represents the total rockfall activity near in both space and time to the grid cell of interest (x, z) on the date of interest (t), while the denominator represents the maximum possible recorded variable of the numerator (as if a rockfall occurred in each grid cell on each day of monitoring). This normalization ensures that the scale of the STRFD remains consistent from day to day (and from grid cell to grid cell) such that relative values can be appropriately compared; without the presence of the denominator term, Eq. (1) would be biased towards higher values near the center of the outcrop and later in the monitoring period. Note that the calculation of the normalization factor in the denominator by assuming the maximum rockfall activity corresponds to a single rockfall in each cell each day is a practical simplification; in reality, more than one rockfall could theoretically occur in any given cell on any given day.

Singularities exist in Eq. (1) when a rockfall has occurred in the cell of interest and/or on the date of interest. In these cases, the rockfall is treated as if it were one grid cell away (in the former case) or one day in the past (in the latter case). Accordingly, the maximum contribution of any given rockfall to the numerator of the STRFD equation is one.

“a” and “b” represent empirical weighting coefficients that determine how “far” influence of a given rockfall propagates in space and time, respectively. Considering spatial units of meters and temporal units of days, it was initially expected that “a” should be greater than “b,” as we hypothesized that the potential for a given rockfall event to influence rockfall hazard decreases more as one moves “d” meters away from the fall than if “d” days of time pass. To determine specific values of these constants, a calibration exercise was performed based on the knowledge that a significant number of smaller rockfalls occurred around the periphery of a large block prior to when it fell between photos taken on July 3 and 4, 2021 (see the “[Evaluation of a major rockfall event on July 3, 2021](#)” section for a more detailed examination of this event). Therefore, for the purposes of identifying areas of potential rockfall hazard, it was determined that values of “a” and “b” should be selected such that the precursor rockfalls around the periphery of the large event should be highlighted. Based on a manual trial and error process, values of $a = 1.7$ and $b = 0.5$ were determined to be appropriate. Note that these empirical constants are approximate in nature and are expected to be slope-dependent rather than universal. The general principle of the STRFD metric could be applied and tuned for application at other slopes, particularly those where large volume rockfalls occur more frequently, and small precursor falls are expected to be more common.

Results

Observed rockfall activity

Over the course of the study period, a total of 220 rockfalls were identified. Of these, 117 had volumes of greater than 0.01 m^3 that were able to be estimated using the change clouds produced by photogrammetry model analysis (the remainder were smaller falls identified through visual analysis of the raw photographs). Figure 8 shows the annualized magnitude-cumulative-frequency (MCF) for rockfall activity at the site. The lack of any visually apparent “roll-over” effect towards the lower end of volumes suggests that there was no systematic under-sampling (i.e., lack of identification) of rockfalls 0.01 m^3 or greater in volume.

Figure 9 presents the final change map obtained from comparison of the models generated on 2020 January 24 and 2021 November 30. This change map shows a number of rockfalls that occurred during the study period, as well as several areas of noise, typically associated with shadows or block edges; noise is slightly more prevalent near the edges of the model due to minor distortion effects present in the photogrammetric model generation.

Although the cumulative change map shown in Fig. 9 gives some sense of rockfall locations, the presence of noise and lack of information about locations of rockfalls that were too small to be identified from the change map make it an incomplete representation of the spatial distribution of rockfalls on the slope. Therefore, as an alternative visualization, Fig. 10 shows the number of rockfalls

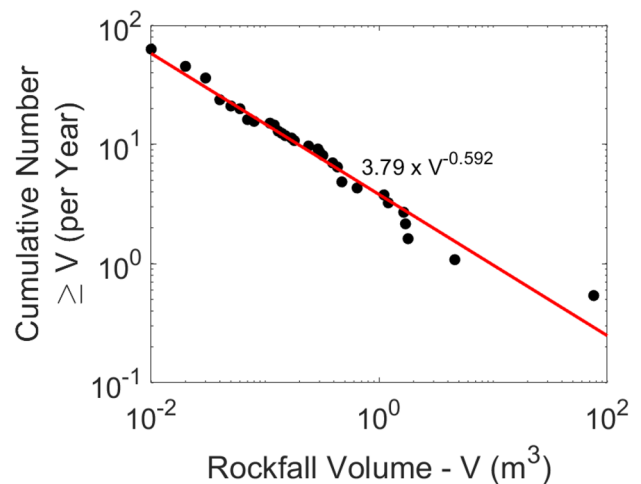


Fig. 8 Magnitude-cumulative-frequency curve with least-squares power law fit overlaid

with centroid in each grid cell (refer to the “[Development of a spatiotemporal rockfall density metric](#)” section). No spatial patterns are immediately obvious, other than perhaps that the thick, massive white sandstone bed near the center of the slope height experiences slightly less rockfall than the surrounding layers.

Of particular interest are the seven largest rockfall events greater than 1 m^3 in volume that occurred during the study period. Photos showing the slope conditions prior to and after each of these events are shown in Fig. 11. The largest event that occurred during the photo interval spanning 2021 July 03 to 2021 July 04 is analyzed in greater detail in the “[Evaluation of a major rockfall event on July 3, 2021](#)” section.

Examination of these photos shows that large rockfalls at the site are associated with some degree of undercutting of weak mudstone layers as well as one or more sub-vertical lateral release planes. It can also be seen that the out-of-plane dimension of these rockfalls is relatively consistent and is controlled by the presence of a sub-vertical cross-joint that is sub-parallel to and set-back from the slope. These observations suggest a combination of wedge, and toppling failure mechanisms are predominant for larger rockfalls at the slope.

Weather influences

When the daily precipitation data are represented in cumulative form and overlain with the cumulative rockfall volume at the site (Fig. 12), two trends become apparent: (1) there is a visually apparent correlation between precipitation and rockfall, and (2) the volume of rockfall during the colder months when freeze–thaw typically occurs (mid-October through mid-April) is minimal. Further comparison of freeze–thaw occurrence to short-term rockfall trends did not reveal any apparent influence of freeze–thaw as a rockfall trigger at the site; specifically, a cross-correlation analysis did not identify any consistent time-lag between individual intervals with freeze–thaw and intervals with rockfall. Accordingly, the results presented in this section focus on the triggering influence of precipitation on rockfall. However, the potential influence of

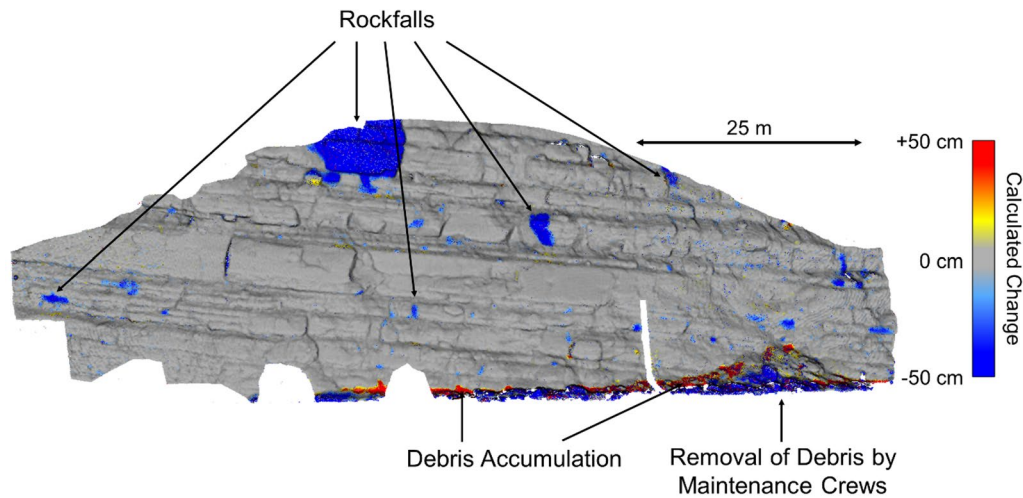


Fig. 9 Annotated change map for the entire study period (note that many smaller rockfalls that are visible are not annotated); change below 5 cm is fully greyed out

freeze–thaw in conditioning the slope to generate rockfall in the following spring and summer months is discussed in the “[Discussion](#)” section.

A threshold-based analysis was conducted whereby the proportions of photo intervals with rockfalls of different sizes were determined considering a variety of precipitation thresholds (in 0.01 in./0.254 mm intervals to match the resolution of the precipitation data). The results (Fig. 13) show that, as expected, the proportion of photo intervals with rockfall increases as the precipitation threshold considered is increased. The consistency of the trends shown is a function of the relatively large dataset used. This trend appears whether considering all rockfalls or only rockfalls above a specified volume threshold. Additionally, the decrease in slope that occurs above 24-h precipitation on the order of 8–20 mm (depending on the range of volumes considered) indicates that the marginal impact of additional precipitation on increasing the likelihood of rockfall is negligible above this threshold. Note that a similar analysis was conducted considering 48-h precipitation (including both the precipitation during the photo interval considered for rockfall and the preceding 24 h), and similar trends were observed, suggesting that short-term antecedent precipitation does not act as a significant trigger of rockfall (above and beyond precipitation within a given photo interval itself).

To evaluate the potential impact of local snowmelt on the slope contributing to the triggering of rockfall, an analysis similar to the one presented in Fig. 13 was conducted separately for days with and without visual evidence of snowmelt on the slope. Although the total proportion of photo intervals with active snowmelt experiencing rockfall was higher than the corresponding value for photo intervals without snowmelt (11.6% versus 6.6%), for every non-zero precipitation threshold, t , days with snowmelt experienced rockfall at a lower rate than those without snowmelt. It should also be noted that the most precipitation that occurred during a day with active snowmelt was approximately 4 mm, and the largest rockfall that occurred on a day with active snowmelt had an estimated volume of 0.04 m³. Taken together, these findings suggest that while local snowmelt on the slope may act to trigger small rockfalls in the absence of precipitation, the overall influence of local snowmelt on rockfall processes at the site is limited relative to that of precipitation.

Although the cumulative representation of the influence of precipitation on rockfall as presented in Fig. 13 is useful, it does not allow one to estimate the likelihood of rockfall occurring within a photo interval during which a specified amount of precipitation occurred. Accordingly, Fig. 14 shows the proportion of photo intervals with rockfall for various ranges of precipitation totals during

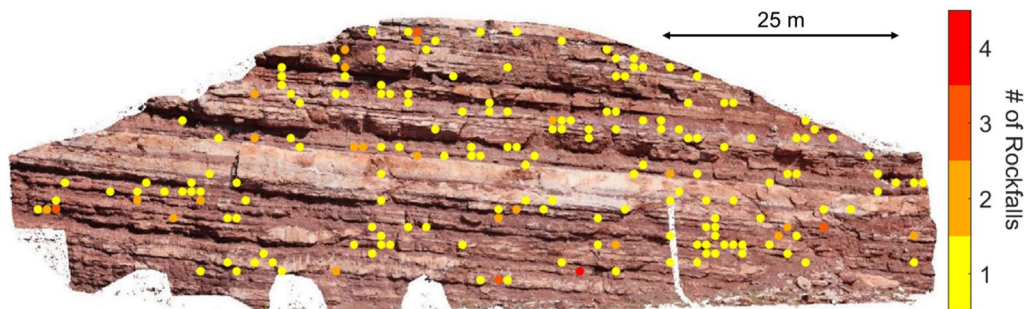


Fig. 10 Spatial distribution of rockfalls shown as number of rockfalls with centroids in each 1 m × 1 m grid cell

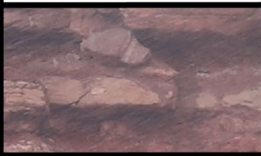













Photo Interval & Volume	Before	After
2021-05-11 to 2021-05-12 1.6 m ³		
2021-07-01 to 2021-07-02 1.1 m ³		
2021-07-01 to 2021-07-02 1.2 m ³		
2021-07-01 to 2021-07-02 1.7 m ³		
2021-07-01 to 2021-07-02 1.8 m ³		
2021-07-03 to 2021-07-04 76 m ³		
2021-09-02 to 2021-09-03 4.6 m ³		

Fig. 11 Before and after photos showing the seven rockfalls with volume > 1 m³ observed during the monitoring period

the same intervals. These results illustrate that the overall trend is for the likelihood of rockfall occurring to increase approximately linearly as a function of precipitation up to a 24-h precipitation total of approximately 15 mm. Note that the decrease in the proportion of photo intervals with rockfall for precipitation totals in the range of 20 to 30 mm is due to the limited number of photo intervals with precipitation observed in this range. Indeed, the results for precipitation totals greater than ~15 mm should be interpreted with caution given the limited sample size.

An alternative way to present the data is to consider how the distribution of 24-h precipitation totals varies for different rockfall cases (Fig. 15). These results show that (1) the vast majority of photo intervals without rockfall also do not have any recorded

precipitation; (2) most photo intervals with rockfall also have some precipitation (50% of such intervals have at least 3 mm of recorded precipitation); (3) the precipitation distribution generally shifts towards higher values when considering larger volume rockfalls. This last finding is consistent with the idea that when a rockfall occurs, its volume may be related to the amount of triggering precipitation. To evaluate this further, the total rockfall volume (sum of all individual volumes) from each photo interval was plotted against the corresponding precipitation value (Fig. 16); note that precipitation was not plotted on a logarithmic axis to allow for the representation of rockfalls that occurred on days with no precipitation.

Figure 17 shows that although precipitation and total rockfall volume tend to increase together, any underlying relationship is

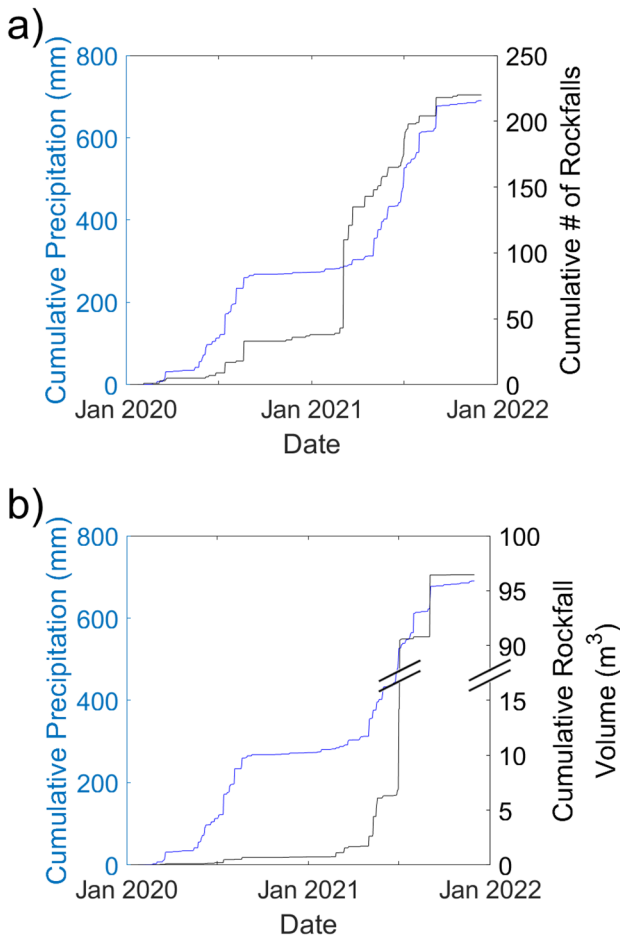


Fig. 12 Cumulative precipitation compared against **a** cumulative number of rockfalls and **b** cumulative rockfall volume (note the axis break associated with the large volume event in July 2021)

highly noisy. Indeed, when testing log-linear and power law models, even when the large (~76 m³) outlier rockfall was excluded, R² values less than 0.2 were obtained despite the models being

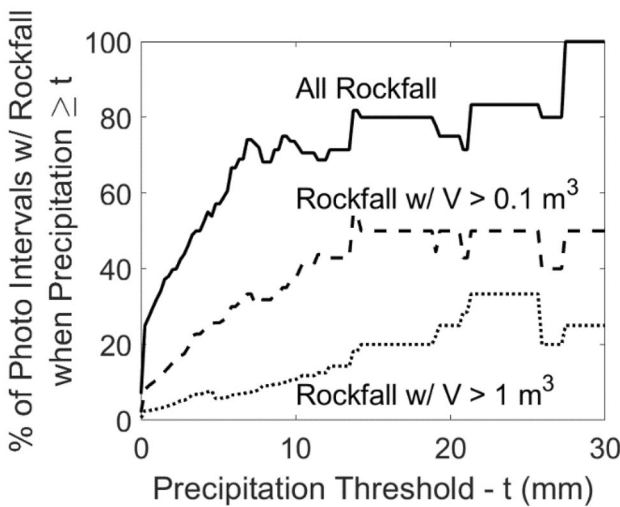


Fig. 13 Percentages of photo intervals with precipitation above a specified threshold, t , that experienced at least one rockfall with a specified minimum volume, V

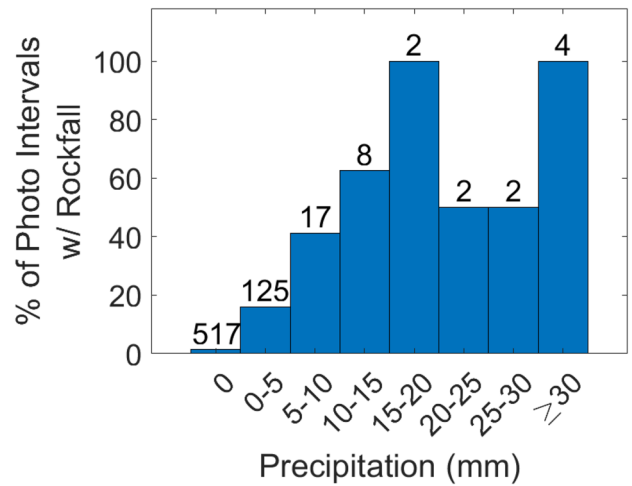


Fig. 14 Proportion of photo intervals that experienced at least one rockfall as a function of the precipitation measured during the same interval; numbers above the bars indicate the total number of intervals in the dataset having precipitation totals within the specified bins

statistically significant ($p < 0.05$). Similar results were obtained when considering the maximum rockfall volume within a given interval as opposed to the total. These findings suggest that although an underlying relationship between precipitation and rockfall volume is likely to exist, this relationship is weak relative to the natural variability present in the rockfall processes considered.

Evaluation of a major rockfall event on July 3, 2021

At around 1:30 pm on July 3, 2021, a ~76 m³ block of rock fell from the monitored slope and resulted in a closure of US-24 during the cleanup of debris (Fig. 17). This was the largest event recorded during the study period. Although the KCOMANIT26 weather station recorded a small amount of precipitation (0.01 in. or 0.254 mm) during same interval as the rockfall, this precipitation

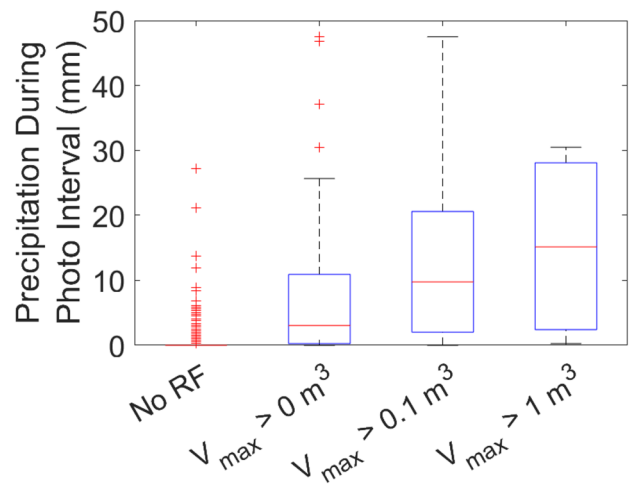


Fig. 15 Boxplots illustrating 24-h precipitation distributions for different rockfall cases

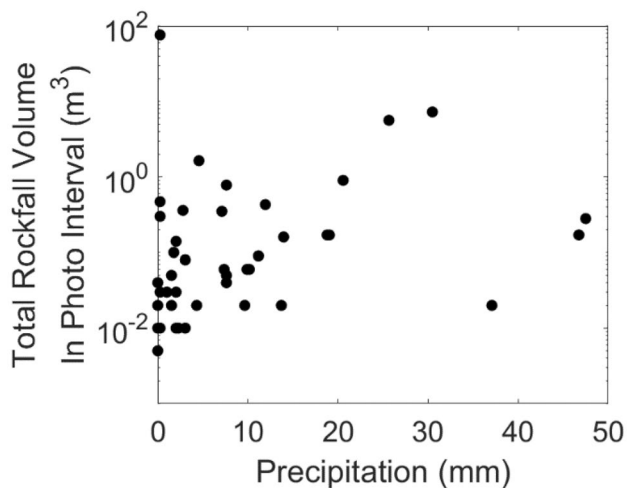


Fig. 16 Semilog plot of total rockfall volume versus precipitation for all photo intervals with rockfall

was actually recorded after the rockfall occurred. The precipitation that occurred most recently prior to the rockfall event was another 0.01 in. (0.254 mm) reading early in the morning of July 2 (around 3 am), over 24 h prior to the rockfall. Accordingly, precipitation was not a key trigger of the rockfall (and it therefore appears as an outlier in Fig. 16).

Similar to many of the other large rockfalls at the site (see Fig. 11), instability occurred due to a combination of undercutting and the presence of sub-vertical lateral fractures bounding the block that ultimately failed. For this particular large rockfall event, the occurrence of a series of smaller rockfalls was critical in loosening the unstable block. Figure 18a shows the sequence of these falls surrounding the larger block, which initiated with the loss of a block from a lower sandstone layer that was holding a previously displaced loose block in place (wedged between the lower layer and

the large rockfall block). Following this, in the week leading up to the large rockfall event, a series of blocks towards the left flank of the large block fell, releasing lateral confinement on the large block; some blocks above the main rockfall block also fell during the same time period; although based on their position, they were unlikely to have had a major effect on the progression of the failure of the large block. Note that all of these smaller falls occurred during photo intervals where precipitation was recorded. Figure 18b shows the state of the block on July 2, where comparison with the earlier photos (e.g., Fig. 18a) reveals some forward toppling motion of the large block (visible even in the two-dimensional raw photographs) as well as downward movement of blocks above the main rockfall block into a growing backscarp; note that these changes are more readily visible when viewing the photos as a GIF (see online supplementary material). We interpret the forward motion of the large block and the surrounding rockfalls to be related, with block motion promoting the occurrence of precursor falls around the block perimeter, and vice versa.

The toppling failure mechanism of the block can be clearly seen in a change map (Fig. 19) comparing photogrammetric models from the start of monitoring (2020 January 24) to just before the rockfall occurred (2021 July 03). Specifically, in addition to the precursor rockfalls being clearly shown in blue, the large block shows outward movements of up to ~10 cm, with a clear gradient from the top of the block to the bottom being indicative of toppling motion.

The evolution of block movement over the months was evaluated by tracking the movement of a single point on the slope (shown as a white circle in Fig. 19) based on the daily change calculation results for the months leading up to the large rockfall (starting on 2021 January 24, 1 year after the start of monitoring). The result, shown in Fig. 20, illustrates that the movement of the block was negligible prior to the May 11–12 precursor fall, suggesting that the rocks below were providing appreciable buttressing support; starting on 2021 July 01, the movement began to accelerate towards failure. In comparing the pre-failure movement to the pre-failure deformation database of Kromer et al. (2018), it can be seen that the total magnitude of

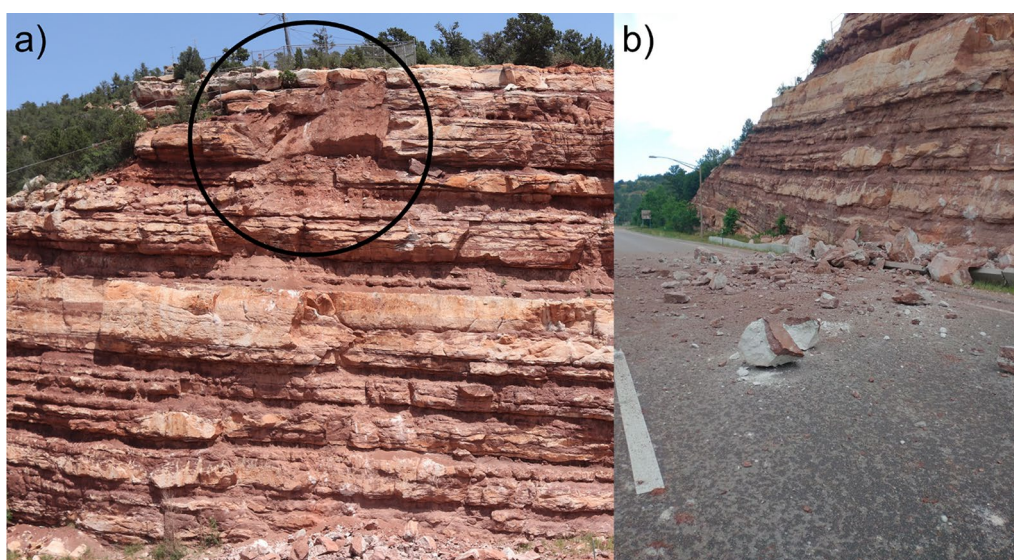


Fig. 17 Post-failure photographs illustrating **a** the source zone scar (circled in black) and **b** rockfall debris on the roadway (photo courtesy CDOT)

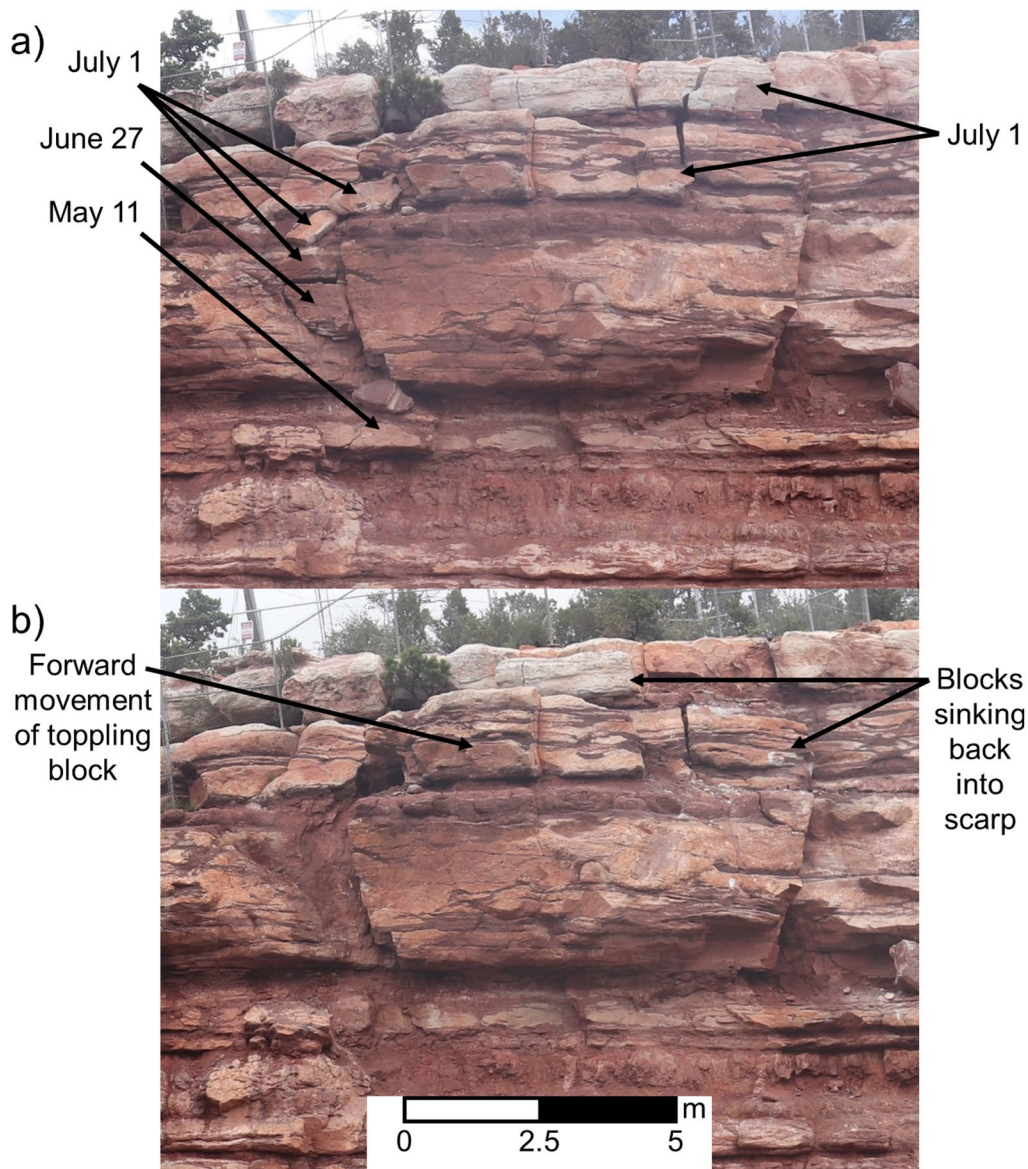


Fig. 18 Photos of the large rockfall block illustrating **a** precursor falls on a photograph from 2021 May 05 (dates correspond to the first date for the photo interval within which each fall occurred) and **b** evidence of failure development on a photograph from 2021 July 02

pre-failure movement is generally consistent with extrapolation of the trend illustrated by Kromer et al. (2018) for smaller toppling blocks; the total duration of pre-failure deformation is much smaller, however (60 days versus a value of several thousand days as predicted by extrapolation of the Kromer et al. (2018) trend). This comparison demonstrates that the characteristics of pre-failure movement can vary significantly from slope to slope depending on factors such as slope morphology, geological setting, and climate (all of which differ between this study and Kromer et al. 2018).

STRFD prior to the July 3, 2021 rockfall event

As stated in the “[Development of a spatiotemporal rockfall density metric](#)” section, the motivation of developing the STRFD metric

was to allow for spatiotemporal clusters of rockfall that might precede large rockfall events to be easily identified. From a practical perspective, regions of high STRFD can be considered as meriting further scrutiny (e.g., detailed examination of change results to look for evidence of nearby forward block movement, field investigation, etc.) but should not be interpreted to indicate that further rockfall is necessarily likely to occur nearby in the near future.

With this in mind, STRFD values were calculated based on all rockfall events that occurred up to the photo interval ending on 2021 July 03 (just prior to the $\sim 76 \text{ m}^3$ rockfall event). In evaluating the raw STRFD results (Fig. 21a), it can be seen that although the rockfall precursors surrounding the large rockfall blocks correspond to areas of relatively high STRFD, there are also several other regions of the slope with similar STRFD values. From a rockfall

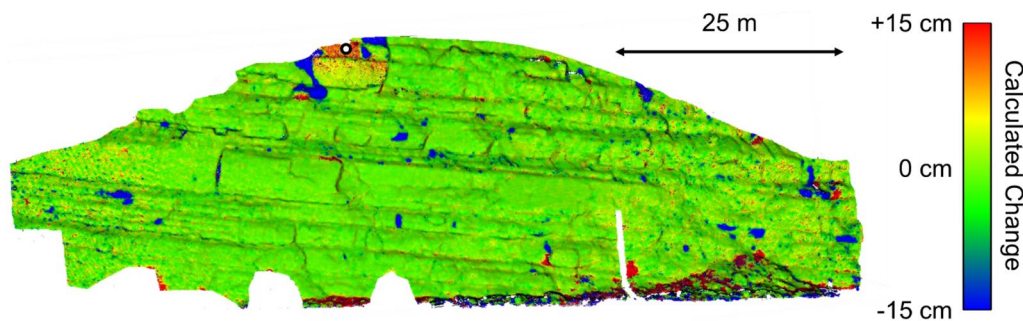


Fig. 19 Change map derived from comparison of photogrammetric models from 2020 January 24 and 2021 July 03; the white circle near the top of the moving block indicates the point tracked to develop the change time series presented in Fig. 20. Note that unlike in Fig. 9, change below 5 cm is not greyed out to allow spatially extensive lower-magnitude change to be observed (e.g., the lower part of the large block)

forecasting perspective, this suggests that the number of “false positive” indications of potential future rockfall activity is high.

As a potential alternative to these STRFD values, a second set of STRFD values was calculated by considering only rockfalls with volume greater than or equal 0.01 m^3 . This alternative calculation was motivated by three factors: (1) the hypothesis that very small rockfalls should be less critical as precursors of large rockfalls; (2) the potential to derive STRFD values automatically in future based solely on larger rockfalls that can be identified directly from the point cloud change maps; (3) the fact that for these larger rockfalls, one can be confident that all such rockfalls on the slope have been detected (per the magnitude-cumulative-frequency curve shown in Fig. 8). In comparing the alternative STRFD values calculated considering a volume threshold (Fig. 21b) to the baseline values (Fig. 21a), it can be seen that the number of slope regions with elevated STRFD is significantly lower; this suggests that many of the “false positives” associated with the original calculation were associated with the occurrence of very small rockfalls. Although one erroneous region of elevated STRFD persists near the bottom left of the monitored area (no large rockfalls occurred in this region of the slope during the monitoring period), the regions corresponding

to precursors of the large July 3, 2021 event more clearly stand out as regions of elevated rockfall activity.

Note that these results are strictly intended to represent a “proof-of-concept” for the STRFD metric. Insufficient data are available to more thoroughly evaluate the metric’s potential value as a rockfall forecasting tool (no other rockfalls associated with precursor rockfall activity were noted during the study period).

Discussion

This study demonstrates the potential use of daily fixed photogrammetric monitoring both to retroactively study rockfall processes and to forecast the potential for future rockfall occurrence. Results provide unique insights into rockfall failure processes, rockfall triggering, and precursor activity based on the long-term and high spatiotemporal resolution of the developed rockfall database. This section addresses each of the research questions identified in the “Introduction” section, including rock slope failure mechanism, rockfall triggers and block size, rockfall precursor analysis, and spatiotemporal evolution of hazard; practical implications for managing rock slope assets are also presented.

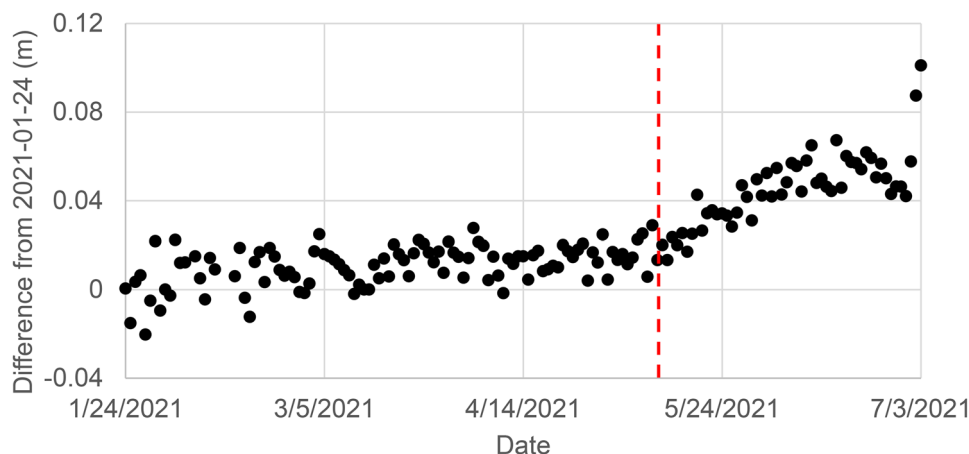


Fig. 20 Pre-failure movement of a point towards the top center of the large (76 m^3) rockfall block that fell on 2021 July 03 (see the white circle in Fig. 19 for the location of the query point used); the dashed red line corresponds to the May 11–12 precursor rockfall

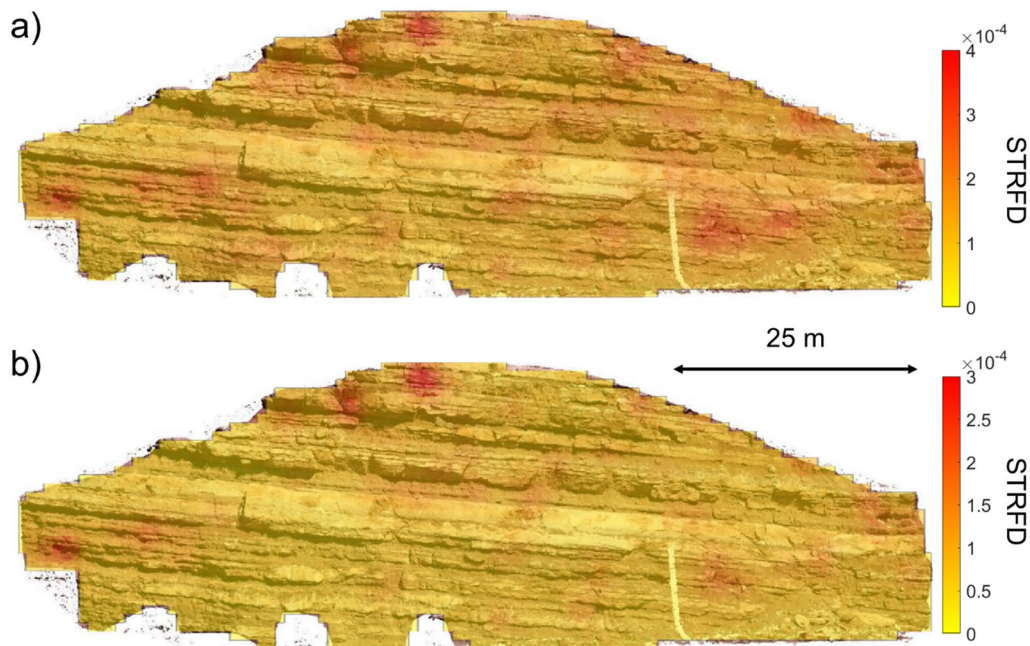


Fig. 21 STRFD values calculated for July 3, 2021 based on rockfalls up to that date using **a** all rockfalls and **b** rockfalls with volume greater than or equal to 0.01 m³; note the difference in color scales (necessary because of the smaller number of rockfalls used to calculate the STRFD (**b**))

Failure mechanisms

Based on the jointing patterns at the studied slope, most of the rockfalls were observed to be associated with wedge sliding or toppling failure mechanisms. Regardless of the overall motion type, it was observed that undercutting of blocks by either erosion (of weaker mudstone layers) or progression of smaller rockfalls (in stronger sandstone layers) likely played a substantial role in destabilizing many of the larger rockfalls that occurred (for example, see Fig. 11).

Triggering and seasonality

The release of potential unstable blocks from the slope was interpreted to be primarily triggered by precipitation, as demonstrated in the “Weather influences” section. It is notable that this influence was generally consistent despite the presence of noise in the data associated with the 24-h resolution of the data set (e.g., cases where precipitation followed a rockfall in the same photo interval, or cases where precipitation occurred leading up to a given rockfall, but in a different photo interval) and the potential for localized precipitation trends to cause discrepancies between precipitation at the monitored slope and at the weather station used. This consistency is attributed to the length of the monitoring timeframe used, and the associated trends may not have been detectable given a shorter monitoring period. The clear triggering influence of precipitation does not mean, however, that rockfall size can be directly linked to the magnitude of a triggering precipitation event. Similar conclusions were reached for a cut slope in metamorphic rock elsewhere in Colorado’s front

range by Malsam (2022) and for natural metamorphic rock slope in a high alpine environment in France by Mourey et al. (2022). It is also important to note that the observation of differences in precipitation triggering of rockfall depending on block volume in this study suggests that findings regarding triggering presented purely in terms of increases in overall rockfall frequency across a large range of volumes may inaccurately represent the influence of precipitation on the largest blocks (which are most relevant to overall erosion rates and hazard management).

Although individual freeze–thaw and local snowmelt events were not found to have any direct influence on the occurrence of individual rockfall at the study site, this should not be interpreted to mean that these processes do not affect the overall rockfall activity of the slope. A more sophisticated approach to account for total liquid inputs, similar to that of Bajni et al. (2021) could have the potential to identify snowmelt impacts that were not detected in this study. Additionally, although the higher rockfall activity observed during the late spring and summer months (Fig. 12) could be attributed to increased precipitation during that time of year, it is also plausible that the slope as a whole is weakened and conditioned for failure by the cumulative effects of the immediately preceding freeze–thaw period (Malsam 2022).

Similar to this study, several studies of rockfall processes in alpine environment climates have found that rockfall activity typically increases during or immediately following the seasonal period of slope thawing (e.g., Matsuoka and Sakai 1999; Paranunzio et al. 2016; Viani et al. 2020). This may be in part associated with the effects of regional (as opposed to local) snowmelt causing groundwater levels to rise and generally pre-dispose the slope to greater rates of rockfall activity during subsequent rockfall events. Another possible explanation is that the thawing of ice in rock joints within

the slope causes a loss of the effective rock joint cohesion that limited rockfall activity during the colder months (D'Amato et al. 2016). To this point, it is relevant to note that the temperature data used to evaluate freeze–thaw cycles for the purposes of this study was air temperature data; in reality, the temperature trends within the slope would be expected to fluctuate much less such that individual diurnal thawing events during colder months would be unlikely to result in thawing of ice within the rockmass that had frozen over a prolonged period of cold temperatures. In terms of the magnitude of the effect, however, in contrast to studies in alpine environments, typical daily high air temperatures are above freezing (see Fig. 6a), meaning the maximum depth of frost penetration in any given year is likely much lower. The lack of single, dominant peak in rockfall activity at our study site during the spring months (as observed in alpine environments) may be in part associated with this more limited depth of freezing.

Studies conducted in milder climates with temperatures more similar to those in Manitou Springs have also tended to find that precipitation acts as key rockfall trigger, to varying degrees (Delonca et al. 2014; Macciotta et al. 2015; D'Amato et al. 2016; Pratt et al. 2019; Maineri et al. 2021; Malsam 2022). However, two key distinctions can be drawn between these other studies and our findings. The first is that a majority of the prior studies identified freeze–thaw as a key short-term rockfall trigger (Delonca et al. 2014; Macciotta et al. 2015; D'Amato et al. 2016; Pratt et al. 2019). The second difference is that studies conducted in regions with substantial rainfall and freeze–thaw during the winter months tended to observe high levels of rockfall activity during these months (e.g. Delonca et al. 2014; Macciotta et al. 2015; D'Amato et al. 2016; Pratt et al. 2019); other study sites either experienced limited freeze–thaw cycling (Maineri et al. 2021) or limited liquid precipitation (Malsam 2022). We interpret this as an indication that an abundance of liquid precipitation available to freeze is critical to allowing freeze–thaw processes to have a substantial impact on rockmass degradation and that the lack of substantial precipitation at the Manitou Springs site during the winter months can explain, at least in part, the lack of a notable freeze–thaw triggering effect. Relatedly, this shifts the period of highest rockfall activity at our site into the spring, summer, and early fall when precipitation totals are highest (almost no rockfall activity was observed during the winter months; see Fig. 12).

Comparison with other rockfall databases

In terms of total rockfall activity, although it is difficult to make precise comparisons with the literature due to differences in slope size (which are not always reported) and rockfall database characteristics, some general comparisons can be made. For example, considering rockfalls in the volume range of 0.01 to 10 m³, we estimated the following values (which were not previously explicitly reported):

- Janeras et al. (2023) observed on the order of 0.0003 rockfalls per year per square meter of natural slope area (“Castellfolli de la Roca”)

- D'Amato et al. (2016) observed on the order of 0.001 rockfalls per year per square meter of natural slope area (“Mont Saint-Eynard”)
- Malsam (2022) observed on the order of 0.002 rockfalls per year per square meter of cut slope area (“Floyd Hill”)
- Kromer et al. (2019) observed on the order of 0.005 rockfalls per year per square meter of cut slope area (“Idaho Springs”)
- Weidner and Walton (2021) observed on the order of 0.005 and 0.01 rockfalls per year per square meter of cut slope area (“E” and “H/I”); note that these are likely upper bound estimates given that they correspond only to data for two April–August periods and exclude the lower rockfall activity fall and winter months as these sites
- The rockfall rate observed in this study corresponds to approximately 0.02 rockfalls per year per square meter of cut slope area.

Although the specific values above are approximate, it is clear that the Manitou Springs slope considered in this study exhibits the highest rate of rockfall activity among those considered. Although many factors may contribute to this difference, we hypothesize that two primary factors explain the increased level of rockfall activity: (1) the slope is a cut slope, meaning that it is by definition oversteepened relative to the geomorphic equilibrium (in contrast to the natural slopes considered by D'Amato et al. 2016 and Janeras et al. 2023); (2) in contrast to the other slopes, which consist of relatively homogeneous basalt (Janeras et al. 2023), limestone (D'Amato et al. 2016), and gneiss (Malsam 2022; Kromer et al. 2019; Weidner and Walton 2021), the presence of heterogeneous weak layering promotes increased occurrence of rockfall due to differential weathering and undercutting. We consider this a preliminary finding that should be further explored in the context of a more comprehensive analysis of natural and cut slopes in differing geological and climatic conditions. Such analysis will become increasingly feasible as the number of published rockfall case studies with high spatiotemporal resolution increases.

Asset management implications

Following the large rockfall on July 3, 2021, protocols for data analysis and visualization were modified accordingly to allow for the system to be used for early detection of potential large events in future. For example, detectability of precursor movement was improved greatly by using a color ramp focused solely on positive change. While it was not possible to detect precursor movements for most of the smaller rockfalls at the site, the detectability of a 76 m³ moving block weeks before detachment using a fixed photogrammetric system is a promising result for this monitoring technology. In contrast, previous studies detecting precursors for blocks of similar size have largely involved the use of terrestrial laser scanning (Abellán et al. 2010; Royan et al. 2015; Kromer et al. 2015) or GB-InSAR (e.g. Carlà et al. 2019). In future, similar fixed photogrammetry systems could potentially be used to provide advanced indication of failure at both natural and cut slopes, allowing preventative measures to be implemented.

In addition to change results, the use of metrics such as the STRFD concept proposed in this paper may ultimately prove useful in identifying areas where spatiotemporal clustering of rockfalls indicate an increased hazard of a larger rockfall event occurring, particularly when used in conjunction with evaluation of slope movement. Such a tool could prove useful in terms of optimizing maintenance activities at monitored slopes. However, significantly more validation and slope-specific parameter calibration is required prior to broader application of the STRFD concept.

From an asset management perspective, daily monitoring can aid in the assessment of natural and cut slope deterioration rates. Precise slope deterioration rates can be determined and extrapolated to analogous slopes in the region. Several representative cut slopes or assets could be monitored in this way, and maintenance programs could be optimized using the data obtained. Overall, this type of monitoring can be used to more accurately model rockfall hazard and to inform mitigation design and maintenance actions.

Conclusions

This study evaluated the rockfall processes and environmental triggering factors at a sedimentary rock cut along US highway 24 in Colorado at a daily monitoring frequency over a 22-month period using a fixed photogrammetry monitoring system. This unique rockfall database is allowed for analysis of small magnitude rockfalls, analysis of rockfall triggers, detection of precursor activity prior to failure, and the development of a spatiotemporal density metric. A total of 220 rockfalls were identified from 2020 January 24 to 2021 November 30, consisting primarily of wedge and toppling failures associated with sub-vertical bounding fractures and undercutting of weak mudstone interbeds. Although precipitation was determined to be the primary triggering factor for rockfall, the relationship between precipitation within a given 24-h monitoring interval and the corresponding total rockfall volume within the same interval was found to be relatively weak; in other words, increased precipitation increased the likelihood of rockfall occurrence, but not necessarily the rockfall volume. Additionally, the marginal influence of additional precipitation on overall rockfall occurrence beyond 8 mm in a given day was found to be limited. This threshold was found to be higher for larger rockfalls, however; the differences in effects of precipitation on triggering of rockfalls of different sizes suggest that an approach of simply quantifying precipitation-induced increases in overall rockfall frequency across a large range of volumes may inaccurately represent the influence of precipitation on the largest (and most practically relevant) blocks. No direct influences of freeze–thaw or snowmelt were identified, but these factors were interpreted to contribute to slope conditioning and increased rockfall rates during the late spring and summer months.

A detailed post-failure analysis of a 76 m³ rock detachment revealed several detectable precursor indicators prior to failure. Toppling motion was found to initiate upon the loss of a rock below providing buttressing support. Subsequent precursor falls removed lateral confinement from the block and allowed movement to accelerate. Although the precursor falls were interpreted to have been triggered by precipitation events, the large rockfall event itself occurred as a progressive failure independent of precipitation immediately prior to block release. The ability of fixed photogrammetry systems to detect precursor movement at a

relatively low operating cost (due to full automation) could have wider implications for improving safety and performance of rock slope assets along transportation corridors worldwide. The addition of a spatiotemporal rockfall density metric could also be used to guide rockfall maintenance/mitigation activities. For example, areas showing precursor movement or high spatiotemporal density could be scheduled for scaling or stabilizing work. Furthermore, to effectively manage rock slope assets along transportation corridors, detailed models for deterioration rates are necessary, such as the ones being developed in this study. In this case, a better understanding of sedimentary rock slope deterioration rates and slope failure mechanisms could help optimize maintenance timing and activity at similar slopes. While it may not be possible or necessary to implement such systems ubiquitously throughout a corridor, targeted monitoring of representative or high-risk slopes could enhance our understanding of slope processes and our ability to improve rock slope asset performance.

Acknowledgements

BGC employees Alvaro Puento and Jake Genskow who assisted with system design and installation and basic data processing are gratefully acknowledged. Dr. Luke Weidner provided helpful suggestions regarding studies to consider in conducting the literature review, and Dr. Ted Matheson provided information regarding the geological context of the study site.

Funding

Data collection and analysis for this study were funded by the Colorado Department of Transportation.

Data availability

Please contact the corresponding author (gwalton@mines.edu) with any data requests.

Declarations

Competing interests The authors declare no competing interests.

References

- Abellán A, Calvet J, Vilaplana JM, Blanchard J (2010) Detection and spatial prediction of rockfalls by means of terrestrial laser scanner monitoring. *Geomorphology* 119(3–4):162–171. <https://doi.org/10.1016/j.geomorph.2010.03.016>
- Abellán A, Oppikofer T, Jaboyedoff M, Rosser NJ, Lim M, Lato MJ (2014) Terrestrial laser scanning of rock slope instabilities. *Earth Surf Proc Land* 39(1):80–97. <https://doi.org/10.1002/esp.3493>
- Ambient Weather (2018) WS-2902 WiFi OSPREY Solar Powered Wireless Weather Station User Manual. <https://ambientweather.com/mwdownloads/download/link/id/567/>. Accessed 19 July 2022.
- Anders K, Winiwarter L, Lindenbergh R, Williams JG, Vos SE, Höfle B (2020) 4D objects-by-change: spatiotemporal segmentation of geomorphic surface change from LiDAR time series. *ISPRS J Photogramm Remote Sens* 159:352–363. <https://doi.org/10.1016/j.isprsjprs.2019.11.025>
- Anders K, Winiwarter L, Mara H, Lindenbergh R, Vos SE, Höfle B (2021) Fully automatic spatiotemporal segmentation of 3D LiDAR time series for the extraction of natural surface changes. *ISPRS J Photogramm Remote Sens* 173:297–308. <https://doi.org/10.1016/j.isprsjprs.2021.01.015>
- Banji G, Camera CAS, Apuani T (2021) Deciphering meteorological influencing factors for alpine rockfalls: a case study in Aosta

- Valley. *Landslides* 18:3279–3298. <https://doi.org/10.1007/s10346-021-01697-3>
- Birien T, Gauthier F (2023) Assessing the relationship between weather conditions and rockfall using terrestrial laser scanning to improve risk management. *Nat Hazard* 23(1):343–360. <https://doi.org/10.5194/nhess-23-343-2023>
- Blanch X, Abellan A, Guinau M (2020) Point cloud stacking: a workflow to enhance 3D monitoring capabilities using time-lapse cameras. *Remote Sens* 12(8):1240. <https://doi.org/10.3390/rs12081240>
- Blanch X, Eltner A, Guinau M, Abellan A (2021) Multi-epoch and multi-imagery (MEMI) photogrammetric workflow for enhanced change detection using time-lapse cameras. *Remote Sens* 13(8):1460. <https://doi.org/10.3390/rs13081460>
- Calliò D, Mineo S, Pappalardo G (2023) Digital rock mass analysis for the evaluation of rockfall magnitude at poorly accessible cliffs. *Remote Sens* 15(6). <https://doi.org/10.3390/rs15061515>
- Carlà T, Nolesini T, Solari L, Rivolta C, Dei Cas L, Casagli N (2019) Rockfall forecasting and risk management along a major transportation corridor in the Alps through ground-based radar interferometry. *Landslides* 16:1425–1435. <https://doi.org/10.1007/s10346-019-01190-y>
- CloudCompare (version 2.10.2) [GPL software]. (2019). Retrieved from <http://www.cloudcompare.org/>
- D'Amato J, Hantz D, Guerin A, Jaboyedoff M, Baillet L, Mariscal A (2016) Influence of meteorological factors on rockfall occurrence in a middle mountain limestone cliff. *Nat Hazard* 16(3):719–735. <https://doi.org/10.5194/nhess-16-719-2016>
- Delonca A, Gunzburger Y, Verdel T (2014) Statistical correlation between meteorological and rockfall databases. *Nat Hazard* 14(8):1953–1964. <https://doi.org/10.5194/nhess-14-1953-2014,2014>
- DiFrancesco PM, Bonneau DA, Hutchinson DJ (2021) Computational geometry-based surface reconstruction for volume estimation: a case study on magnitude-frequency relations for a LiDAR-derived rockfall inventory. *ISPRS Int J Geo Inf* 10(3):157. <https://doi.org/10.3390/ijgi10030157>
- Eltner A, Kaiser A, Castillo C, Rock G, Neugirg F, Abellán A (2016) Image-based surface reconstruction in geomorphometry—merits, limits and developments. *Earth Surf Dyn* 4(2):359–389. <https://doi.org/10.5194/esurf-4-359-2016>
- Eltner A, Kaiser A, Abellan A, Schindewolf M (2017) Time lapse structure-from-motion photogrammetry for continuous geomorphic monitoring. *Earth Surf Proc Land* 42(14):2240–2253. <https://doi.org/10.1002/esp.4178>
- Esri; Garmin; USGS; NPS. World Reference Overlay. Created 2009, Updated 2019. Available online: https://server.arcgisonline.com/ArcGIS/rest/services/Reference/World_Reference_Overlay/MapServer (accessed on 8 June 2022).
- Fleischer F, Haas F, Altmann M, Rom J, Ressler C, Becht M (2023) Glaciogenic periglacial landform in the making—geomorphological evolution of a rockfall on a small glacier in the Horlachtal, Stubai Alps, Austria. *Remote Sens* 15(6). <https://doi.org/10.3390/rs15061472>
- Gallo IG, Martínez-Corbella M, Sarro R, Iovine G, López-Vinielles J, Hernández M, ... García-Davalillo JC (2021) An integration of UAV-based photogrammetry and 3D modelling for rockfall hazard assessment: the Cárcavos case in 2018 (Spain). *Remote Sens* 13(17). <https://doi.org/10.3390/rs13173450>
- Giacomini A, Thoeni K, Santise M, Diotri F, Booth S, Fityus S, Roncella R (2020) Temporal-spatial frequency rockfall data from open-pit highwalls using a low-cost monitoring system. *Remote Sensing* 12(15):2459. <https://doi.org/10.3390/rs12152459>
- Graber A, Santi P (2023) UAV-photogrammetry rockfall monitoring of natural slopes in Glenwood Canyon, CO, USA: background activity and post-wildfire impacts. *Landslides* 20(2):229–248. <https://doi.org/10.1007/s10346-022-01974-9>
- Guerin A, Stock GM, Radue MJ, Jaboyedoff M, Collins BD, Matasci B, ... Derron, MH (2020) Quantifying 40 years of rockfall activity in Yosemite Valley with historical structure-from-motion photogrammetry and terrestrial laser scanning. *Geomorphology* 356. <https://doi.org/10.1016/j.geomorph.2020.107069>
- Hartmeyer I, Delleske R, Keuschnig M, Krautblatter M, Lang A, Schrott L, Otto JC (2020) Current glacier recession causes significant rockfall increase: the immediate paraglacial response of deglaciating cirque walls. *Earth Surf Dyn* 8(3):729–751. <https://doi.org/10.5194/esurf-8-729-2020>
- Imaizumi F, Trappmann D, Matsuoka N, Cánovas JAB, Yasue K, Stoffel M (2020) Interpreting rockfall activity on an outcrop–talus slope system in the southern Japanese Alps using an integrated survey approach. *Geomorphology* 371. <https://doi.org/10.1016/j.geomorph.2020.107456>
- ISRM (1978) Suggested method for the quantitative description of discontinuities in rock mass. *Int J Rock Mech Min Sci Geomech Abstr* 15:319–368
- James MR, Robson S, Smith MW (2017) 3-D uncertainty-based topographic change detection with structure-from-motion photogrammetry: precision maps for ground control and directly georeferenced surveys. *Earth Surf Proc Land* 42(12):1769–1788. <https://doi.org/10.1002/esp.4125>
- Janeras M, Lantada N, Núñez-Andrés MA, Hantz D, Pedraza O, Cornejo R, ... Palau J (2023) Rockfall magnitude–frequency relationship based on multi-source data from monitoring and inventory. *Remote Sens* 15(8). <https://doi.org/10.3390/rs15081981>
- Kromer RA, Hutchinson DJ, Lato MJ, Gauthier D, Edwards T (2015) Identifying rock slope failure precursors using LiDAR for transportation corridor hazard management. *Eng Geol* 195:93–103. <https://doi.org/10.1016/j.enggeo.2015.05.012>
- Kromer RA, Abellán A, Hutchinson DJ, Lato M, Chanut MA, Dubois L, Jaboyedoff M (2017) Automated terrestrial laser scanning with near-real-time change detection—monitoring of the Séchilienne landslide. *Earth Surf Dyn* 5(2):293–310. <https://doi.org/10.5194/esurf-5-293-2017>
- Kromer RA, Rowe E, Hutchinson J, Lato M, Abellán A (2018) Rockfall risk management using a pre-failure deformation database. *Landslides* 15(5):847–858. <https://doi.org/10.1007/s10346-017-0921-9>
- Kromer R, Walton G, Gray B, Lato M, Group R (2019) Development and optimization of an automated fixed-location time lapse photogrammetric rock slope monitoring system. *Remote Sensing* 11(16):1890. <https://doi.org/10.3390/rs11161890>
- Macciotta R, Martin CD, Edwards T, Cruden DM, Keegan T (2015) Quantifying weather conditions for rock fall hazard management. *Georisk: Assess Manage Risk Eng Sys Geohazards* 9(3):71–186. <https://doi.org/10.1080/17499518.2015.1061673>
- Mainieri R, Eckert N, Corona C, Lopez-Saez J, Stoffel M, Bourrier F (2023) Limited impacts of global warming on rockfall activity at low elevations: insights from two calcareous cliffs from the French Prealps. *Progress in Physical Geography: Earth and Environment* 47(1):50–73. <https://doi.org/10.1177/03091333221107624>
- Mainieri R, Corona C, Lopez-Saez J, Stoffel M, Toe D, Dupire S, ... Bourrier F (2021) Improved tree-ring sampling strategy enhances the detection of key meteorological drivers of rockfall activity. *Catena* 201. <https://doi.org/10.1016/j.catena.2021.105179>
- Malsam A (2022) Characterization of rockfall activity and identification of weather-rockfall relationships using high temporal resolution remote sensing methods. Masters Thesis, Colorado School of Mines
- Matsuoka N (2019) A multi-method monitoring of timing, magnitude and origin of rockfall activity in the Japanese Alps. *Geomorphology* 336:65–76. <https://doi.org/10.1016/j.geomorph.2019.03.023>
- Matsuoka N, Sakai H (1999) Rockfall activity from an alpine cliff during thawing periods. *Geomorphology* 28(3–4):309–328. [https://doi.org/10.1016/S0169-555X\(98\)00116-0](https://doi.org/10.1016/S0169-555X(98)00116-0)
- Mourey J, Lacroix P, Duvillard P-A, Marsy G, Marcer M, Malet E, Ravanel L (2022) Multi-method monitoring of rockfall activity along the classic route up Mont Blanc (4809 m a.s.l.) to encourage adaptation by mountaineers. *Nat Hazard* 22:445–460. <https://doi.org/10.5194/nhess-22-445-2022>
- NOAA (2022) JetStream Max: Addition Köppen-Geiger Climate Subdivisions. *Nat Weather Serv*. https://www.weather.gov/jetstream/climate_max. Accessed 5/17/2023.
- Núñez-Andrés MA, Prades-Valls A, Matas G, Buil F, Lantada N (2023) New approach for photogrammetric rock slope premonitory movements monitoring. *Remote Sens* 15(2). <https://doi.org/10.3390/rs15020293>

- Paranunzio R, Laio F, Chiarle M, Nigrelli G, Guzzetti F (2016) Climate anomalies associated with the occurrence of rockfalls at high-elevation in the Italian Alps. *Nat Hazard* 16(9):2085–2106. <https://doi.org/10.5194/nhess-16-2085-2016>
- Parente L, Chandler JH, Dixon N (2019) Optimising the quality of an SfM-MVS slope monitoring system using fixed cameras. *Photogram Rec* 34(168):408–427. <https://doi.org/10.1111/phor.12288>
- Pratt C, Macciotta R, Hendry M (2019) Quantitative relationship between weather seasonality and rock fall occurrences north of Hope, BC, Canada. *Bull Eng Geol Env* 78(5):3239–3251. <https://doi.org/10.1007/s10064-018-1358-7>
- Robiati C, Mastrantoni G, Francioni M, Eyre M, Coggan J, Mazzanti P (2023) Contribution of high-resolution virtual outcrop models for the definition of rockfall activity and associated hazard modelling. *Land* 12(1). <https://doi.org/10.3390/land12010191>
- Roncella R, Forlani G (2015) A fixed terrestrial photogrammetric system for landslide monitoring. In: *Modern technologies for landslide monitoring and prediction*. Springer, Berlin, Heidelberg 43–67. https://doi.org/10.1007/978-3-662-45931-7_3
- Rosser N, Lim M, Petley D, Dunning S, Allison R (2007) Patterns of precursory rockfall prior to slope failure. *J Geophys Res: Earth Surf* 112(F4). <https://doi.org/10.1029/2006JF000642>
- Royán MJ, Abellán A, Jaboyedoff M, Vilaplana JM, Calvet J (2014) Spatio-temporal analysis of rockfall pre-failure deformation using terrestrial LiDAR. *Landslides* 11(4):697–709. <https://doi.org/10.1007/s10346-013-0442-0>
- Royán MJ, Abellán A, Vilaplana JM (2015) Progressive failure leading to the 3 December 2013 rockfall at Puigcercós scarp (Catalonia, Spain). *Landslides* 12(3):585–595. <https://doi.org/10.1007/s10346-015-0573-6>
- Salvini R, Mastrococo G, Seddaiu M, Rossi D, Vanneschi C (2017) The use of an unmanned aerial vehicle for fracture mapping within a marble quarry (Carrara, Italy): photogrammetry and discrete fracture network modelling. *Geomat Nat Haz Risk* 8(1):34–52. <https://doi.org/10.1080/19475705.2016.1199053>
- Santise M, Thoeni K, Roncella R, Sloan SW, Giacomini A (2017) Preliminary tests of a new low-cost photogrammetric system. *The International Archives of Photogrammetry, Remote Sensing and Spatial Information Sciences* 42:229. <https://doi.org/10.5194/isprs-archives-XLII-2-W8-229-2017>
- Sarro R, Riquelme A, García-Davalillo JC, Mateos RM, Tomás R, Pastor JL, ... Herrera, G (2018) Rockfall simulation based on UAV photogrammetry data obtained during an emergency declaration: application at a cultural heritage site. *Remote Sens* 10(12). <https://doi.org/10.3390/rs10121923>
- Śledź S, Ewertowski MW, Piekarczyk J (2021) Applications of unmanned aerial vehicle (UAV) surveys and structure from motion photogrammetry in glacial and periglacial geomorphology. *Geomorphology* 378. <https://doi.org/10.1016/j.geomorph.2021.107620>
- Stoffel M, Schneuwly D, Bollschweiler M, Lievre I, Delaloye R, Myint M, Monbaron M (2005) Analyzing rockfall activity (1600–2002) in a protection forest—a case study using dendrogeomorphology. *Geomorphology* 68(3–4):224–241. <https://doi.org/10.1016/j.geomorph.2004.11.017>
- Sweet DE, Carsrud CR, Watters AJ (2015) Proposing an entirely Pennsylvanian age for the Fountain Formation through new lithostratigraphic correlation along the Front Range. *The Mountain Geologist* 52(2):43–70
- USGS. Search Earthquake Catalog. 2022. Available online: <https://earthquake.usgs.gov/earthquakes/search/> (accessed on 19 July 2022).
- van Veen M, Hutchinson DJ, Kromer R, Lato M, Edwards T (2017) Effects of sampling interval on the frequency-magnitude relationship of rockfalls detected from terrestrial laser scanning using semi-automated methods. *Landslides* 14(5):1579–1592. <https://doi.org/10.1007/s10346-017-0801-3>
- Vanneschi C, Di Camillo M, Aiello E, Bonciani F, Salvini R (2019) SFM-MVS photogrammetry for rockfall analysis and hazard assessment along the ancient roman via Flaminia road at the Furlo gorge (Italy). *ISPRS Int J Geo-Inf* 8(8). <https://doi.org/10.3390/ijgi8080325>
- Viani C, Chiarle M, Paranunzio R, Merlone A, Musacchio C, Coppa G, Nigrelli G (2020) An integrated approach to investigate climate-driven rockfall occurrence in high alpine slopes: the Bessanese glacial basin, Western Italian Alps. *J Mt Sci* 17(11):2591–2610. <https://doi.org/10.1007/s11629-020-6216-y>
- Weather Underground. Manitou Springs, CO Weather History. Available online: <https://www.wunderground.com/history/daily/us/co/manitou-springs/KCOMANIT26> (accessed on 10 December 2021).
- Weidner L, Walton G (2021) Monitoring the effects of slope hazard mitigation and weather on rockfall along a Colorado highway using terrestrial laser scanning. *Remote Sensing* 13(22):4584. <https://doi.org/10.3390/rs13224584>
- Williams JG, Rosser NJ, Hardy RJ, Brain MJ (2019) The importance of monitoring interval for rockfall magnitude-frequency estimation. *J Geophys Res Earth Surf* 124(12):2841–2853. <https://doi.org/10.1029/2019JF005225>
- Zielonka A, Wrońska-Wałach D (2019) Can we distinguish meteorological conditions associated with rockfall activity using dendrochronological analysis? - An example from the Tatra Mountains (Southern Poland). *Sci Total Environ* 662:422–433. <https://doi.org/10.1016/j.scitotenv.2019.01.243>

Springer Nature or its licensor (e.g. a society or other partner) holds exclusive rights to this article under a publishing agreement with the author(s) or other rightsholder(s); author self-archiving of the accepted manuscript version of this article is solely governed by the terms of such publishing agreement and applicable law.

Supplementary Information The online version contains supplementary material available at <https://doi.org/10.1007/s10346-023-02121-8>.

G. Walton (✉) · **R. Kromer** · **A. Silaev**

Department of Geology and Geological Engineering, Colorado School of Mines, Golden, CO, USA
Email: gwalton@mines.edu

C. Christiansen

BGC Engineering, Golden, CO, USA

R. Kromer

University of Leeds, Leeds, UK

A. Silaev

Stantec, Denver, CO, USA